# SCIENTIFIC REP🅾RTS

**OPEN**

# Terahertz detectors arrays based on orderly aligned InN nanowires

Xuechen Chen[1,2], Huiqiang Liu[3], Qiuguo Li[1], Hao Chen[1], Rufang Peng[3], Sheng Chu[1] & Binbin Cheng[4]

Nanostructured terahertz detectors employing a single semiconducting nanowire or graphene sheet have recently generated considerable interest as an alternative to existing THz technologies, for their merit on the ease of fabrication and above-room-temperature operation. However, the lack of alignment in nanostructure device hindered their potential toward practical applications. The present work reports ordered terahertz detectors arrays based on neatly aligned InN nanowires. The InN nanostructures (nanowires and nano-necklaces) were achieved by chemical vapor deposition growth, and then InN nanowires were successfully transferred and aligned into micrometer-sized groups by a "transfer-printing" method. Field effect transistors on aligned nanowires were fabricated and tested for terahertz detection purpose. The detector showed good photoresponse as well as low noise level. Besides, dense arrays of such detectors were also fabricated, which rendered a peak responsivity of 1.1 V/W from 7 detectors connected in series.

The terahertz (THz) radiation region is defined by the frequency range of 0.1 to 10 THz. This range contains abundant physical and chemical information of most substances, making great benefits to vast applications such as interstellar observation, homeland security, as well as medical diagnosis[1,2]. Under this context, much effort has been devoted to achieve high-efficiency, low-cost, and room temperature THz sources and detectors. On the source side, recently miniaturized THz quantum cascade lasers (QCL)[3] and photoconductive THz emitters[4,5] have shown good progress in both output power and operation temperature.

On the detector side, there already exist many THz detection solutions, such as bolometers[6], Schottky diode detectors[7], and field effect transistors (FETs), etc. Among them, plasmon wave detection based on FETs[8,9] possesses several advantages in terms of room temperature operation, wide detection range, and compactness for light-weight on-chip array technologies. In this case, recently a novel approach for simple structured FET detectors by integrating semiconductor nanowires (or graphene) as active elements[10] has been developed and showed good sign of promise. In those devices, a non-resonant broad band detection mechanism often arises because plasma oscillations are normally overdamped in the nanowire channel ($\omega_0 \tau \ll 1$, where $\omega_0$ is the fundamental plasma frequency and $\tau$ is the momentum relaxation time)[11], which can lead to a measurable signal between source and drain electrodes.

Several nanomaterials have been fabricated into THz FET detectors, including InAs[11,12], InSb[13], graphene[14], and ZnO[15]. InN thin films and nanowires, on the other hand, are considered as promising candidate for efficient THz emitters (photo-Dember type) due to their high peak/saturation drift velocity, and low intervalley scattering rate[16]. In fact, InN has theoretical electron mobility up to 14000 cm$^2$/VS[17], which makes it in principle suitable for THz applications. Hence the development of THz detectors based on InN nanowires is of strong interest. Here in this contribution, an systematic investigation was made on the material synthesis, nanowire alignment, device fabrication, device arrays integration and THz

[1]State Key Laboratory of Optoelectronic Materials and Technology, Sun Yat-Sen University, Guangdong Guangzhou 510275, China. [2]School of Mobile Information Engineering, Sun Yat-Sen University, Guangdong Guangzhou 510275, China. [3]State Key Laboratory Cultivation Base for Nonmetal Composites and Functional Materials, Southwest University of Science and Technology, Sichuan Mianyang 621010, China. [4]Institute of Electrical Engineering, Chinese Academy of Engineering Physics, Mianyang 621423, China. Correspondence and requests for materials should be addressed to S.C. (email: chusheng@mail.sysu.edu.cn) or B.C. (email: chengbinbin@tsinghua.org.cn)

characterizations for InN nanomaterial. On the growth section, it is found that during InN nanowire growth, another material form nano-necklace was formed simultaneously. Then the crystal properties and growth mechanisms were studied in detail. For device demonstration, especially instead of conventional single nanowire device geometry, THz detectors were fabricated from several aligned nanowires. THz detectors array was further realized by integration individual nanowires-device in series. The advantages of this approach lies in: 1. only nanowires with controlled density, position, as well as orientation will likely find ultimate applications. 2. THz wave has typical focus spot larger than $100\,\mu m$. If more than one subwavelength sized devices are connected, stronger photoresponse can be generated. Hence in the fabrication process we adopted a "transfer printing" approach developed by others[18,19], which enabled alignment of groups consist 3 to 6 InN nanowires into designed areas for subsequent device fabrication. The result of these devices unequivocally demonstrates fairly good FET properties of the multi-nanowires sample, which successfully produced sum responsivity of 1.1 V/W from integrated device arrays. This result is important for many THz applications.

## Results

The InN nanostructures were prepared by chemical vapor deposition (CVD) method. Although the growth was intentionally designed for only nanowires, however, distinctly, after growth there were two kinds of InN morphologies seen on the as-grown substrate: nanowires and "nano-necklace". It is then found that the places close to the source grow nanowires whereas further away positions were covered mostly by nano-necklace. Fig. 1a,b are the scanning electron microscope (SEM) images of InN nanowires and nano-necklaces on close and far parts (to the source) of the substrate, respectively. The co-existence of different morphologies suggests that the growth of various InN nanostructures in CVD has narrow growth windows. Thus, slight variation of growth parameter (such as III/V ratio) can yield drastic different growth modes. In addition, the heads or parts of these nanomaterials do not contain gold nano-particles (method section) in SEM images, indicating the vapor-solid growth mode[20]. The role of gold nanoparticles prior to the growth is to increase the surface roughness to facilitate vapor nucleation. Magnified SEM image of a typical InN nano-necklace architecture is shown in Fig. 1c, which exhibits clearly that the typical nano-necklace consists of a number of connected and uniform beads. The major and minor waists range from 200 to 400 and 200 to 1000 nm, respectively.

The crystal structure of the as-obtained product was characterized by X-ray diffraction (XRD) (Fig. 2). All of the strong reflection peaks can be indexed to wurtzite-type InN (w-InN). According to the Bragg equation ($2d\sin\theta = \lambda$) and interplanar spacing formula $\left( d = \frac{a}{\sqrt{\frac{4}{3}(h^2 + hk + k^2) + \left(\frac{a}{c}\right)^2 l^2}} \right)$, where $d$, $\theta$, $\lambda$, $\{hkl\}$ are the interplanar spacing, diffraction angle, wavelength, indices of crystal face, respectively. The lattice constants can be calculated as: $a = 0.35$ nm and $c = 0.57$ nm (JCPDS card NO. 02-1450), which match well with the (100) and (002) planes of w-InN InN, respectively[21]. XRD peaks related to other phases (such as In and $In_2O_3$) were not found. Energy dispersive spectroscopy (EDS) measurements were performed to determine the chemical composition of the samples. Fig. 3a illustrates a typical SEM image of sample part that found co-existence of InN nano-necklaces and nanowires. The EDS spectrum of marked position in Fig. 3a is shown in Fig. 3b. Distinct In and N peaks were found to confirm the InN elemental composition, while the silicon peak originates from the substrate. Oxygen peak is attributed to $SiO_2$ and Indium oxide related substances. The atomic ratio of In: N is close to 1 : 1, suggesting good stoichiometry of the material.

The chemical composition and microstructure of as-synthesized InN nanostructures were further studied by transmission electron microscope (TEM). The TEM images of single InN nanowire and nano-necklace sample are shown in Fig. 4a,c, respectively. High resolution (HR)-TEM of Fig. 4b is the magnified part of the single nanowire to examine detailed crystal structure. The d-spacing of the lattice fringes measured is 0.28 nm, matching well with the (0001) plane interspacing of wurtzite InN structure. The inset of Fig. 4b shows the corresponding selected area electron diffraction (SAED) pattern taken from the corresponding nanowire, further confirming that the sample is single-crystalline and grows preferentially along the [0001] crystallographic direction. For the InN nano-necklace, Fig. 4c indicates that the nano-necklace consists of multiple single crystalline connected beads, while no grain boundaries between them could be noticed. HRTEM of Fig. 4d (also with fast fourier transfor (FFT) in the inset of Fig. 4d) shows fringe with d-spaces of 0.31 nm. After the TEM studies, the growth pattern of the nano-necklaces can be deduced by the assistance from a w-InN unit cell (Fig. 4e): the growth direction of the nano-necklace is determined to be also [0001]; the equilateral trapezoid facets of the truncated hexagonal beads belong to $\{10\bar{1}1\}$; the edges between two facets are $\langle 2\bar{1}\bar{1}3 \rangle$. By using the standard lattice parameters of w-InN, the angle between two corresponding facets on the opposite sides of the major waist of the beads (e.g. $(10\bar{1}1)$ and $(10\bar{1}\bar{1})$ is calculated to be 124° and that between two corresponding edges (e.g. $[2\bar{1}\bar{1}3]$ and $[2\bar{1}\bar{1}\bar{3}]$) to be 116°. These are in good agreement with the observed values ranging from 116° to 124° in Fig. 4c. The schematic illustration of the nano-necklace is presented in Fig 4e. The fractions of $\{10\bar{1}1\}$ and $\{10\bar{1}\bar{1}\}$ planes are not equal, which may owes to the different polarities of them: the former is In-polar while the later is N-terminated. In other words, the as-obtained nano-necklace (see Figs 1 and 4c) are not exactly the same as simulated Fig. 4e; instead, the $\{10\bar{1}1\}$ planes are more
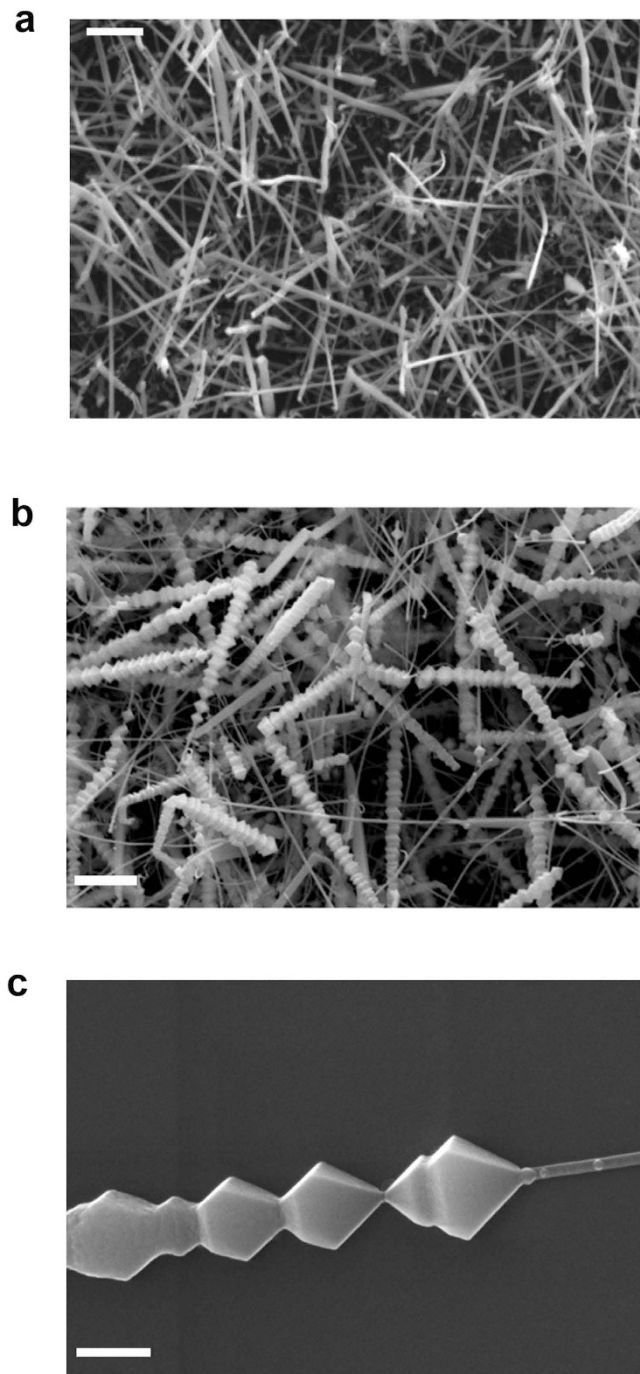
**Figure 1.** FESEM images of the nanowire and nano-necklace structures (**a**) scale bar: 2 μm. (**b**) scale bar: 1 μm. (**c**) Magnified SEM images of a typical InN nano-necklace architectures, scale bar: 300 nm.

favored than the {10$\bar{1}\bar{1}$} ones, which is due to the different formation energies thus different diffusion abilities of the adatoms on these two types of side-surfaces[22]. In addition, similar multi-beads morphologies are also observed in one dimensional hexagonal wurtzite stacked-cone and zigzag AlN[23], GaN[24] and ZnO[25] nanostructures.

The photoluminescence (PL) of the two kinds of structures was carried out (Fig. 5) to investigate the optical properties of single InN nanowire and nano-necklace. The strong emission peaks around 1700 nm can be seen clearly, which corresponds to the near band edge (NBE) emission of InN. This IR-emission peak position is consistent with the NBE emission observed from reported InN nanorods[26] and epitaxial films[27]. Notefully, the emission intensity from the nano-necklace is stronger, and is tentatively attributed
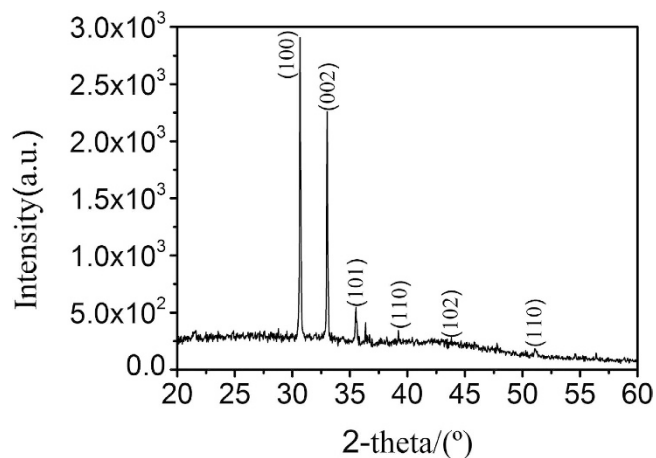
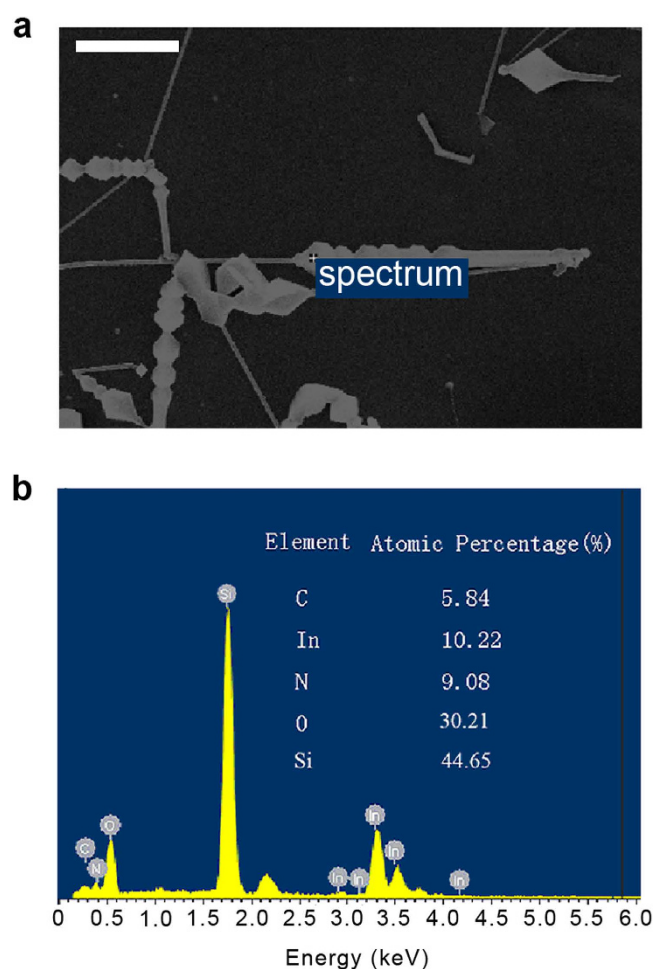**Figure 2. XRD pattern taken on the as-grown InN nanostructures on Si substrate.**



**Figure 3.** (**a**) SEM image of as-synthesized InN nanostructures. scale bar: 1 μm. (**b**) The corresponding EDS spectrum of the InN nanostructures taken at spot spectrum 9 which are marked in (**a**). Inset: the corresponding composition of the nanostructures determined by EDS.

to the larger material size as well as muti-scattering inside one nano-necklace for three dimensional cavity-like light resonant[28].

Although single InN nanowire or nano-necklace can be readily used for THz detectors such like single nanowire FET detectors, randomly distributed nanostructures are less favorable for ultimate practical
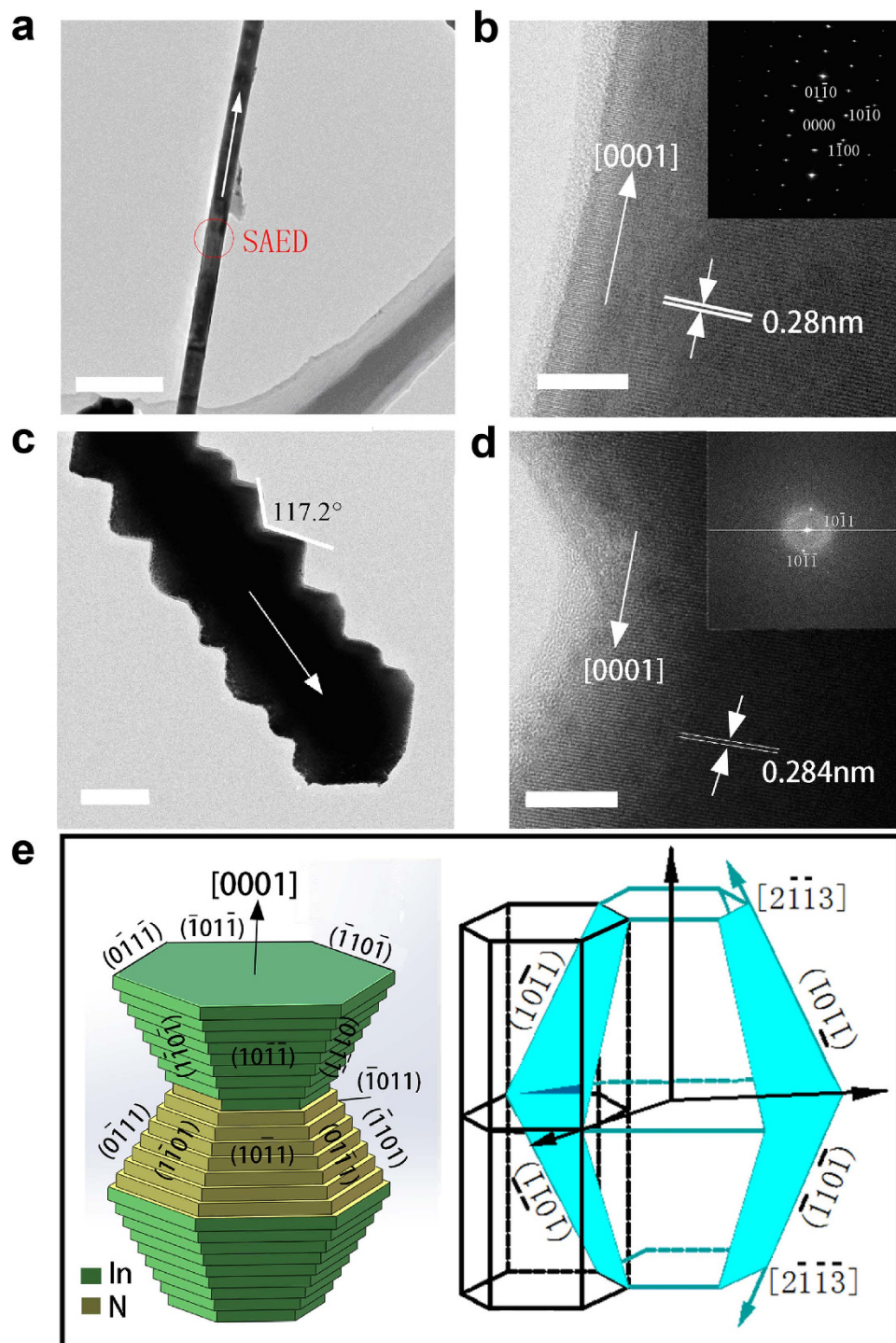
**Figure 4. TEM and HRTEM images of the InN nanowire and InN nano-necklace.** (**a**) TEM image of the individual nanowire, scale bar: 500 nm, (**b**) The corresponding HRTEM image and SAED pattern of the nanowire, scale bar: 10 nm. (**c**) TEM image of the individual nano-necklace, scale bar: 100 nm, (**d**) The corresponding HRTEM image and FFT pattern of the nano-necklace, scale bar: 10 nm. (**e**) Space-filling model of ideal [0001] nano-necklace and schematic of a crystal unit of the w-InN with {10$\bar{1}$1} and {0001} planes enclosed.

applications. For simplicity and wider impact purpose, InN nanowires rather than nano-necklaces were selected to perform alignment and device fabrications. They were transferred from growth Si substrates to a patterned device substrates by a mechanical "transfer printing" process (Fig. 6a). The alignment direction is determined by the mechanic shear force due to relative motion of the two substrates. SEM image of Fig. 6b indicates that 3~6 nanowires can be successfully transferred into trench arrays after
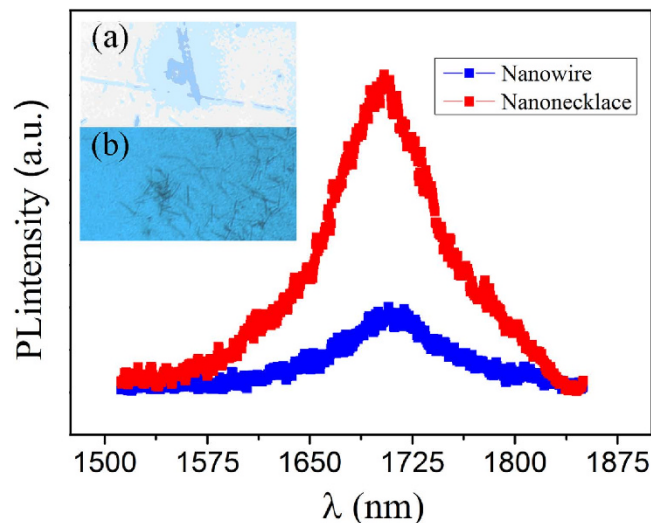
**Figure 5. PL spectra InN nanostructures at room temperature.** The inset shows microscope images of the InN nano-necklaces and nanowires.
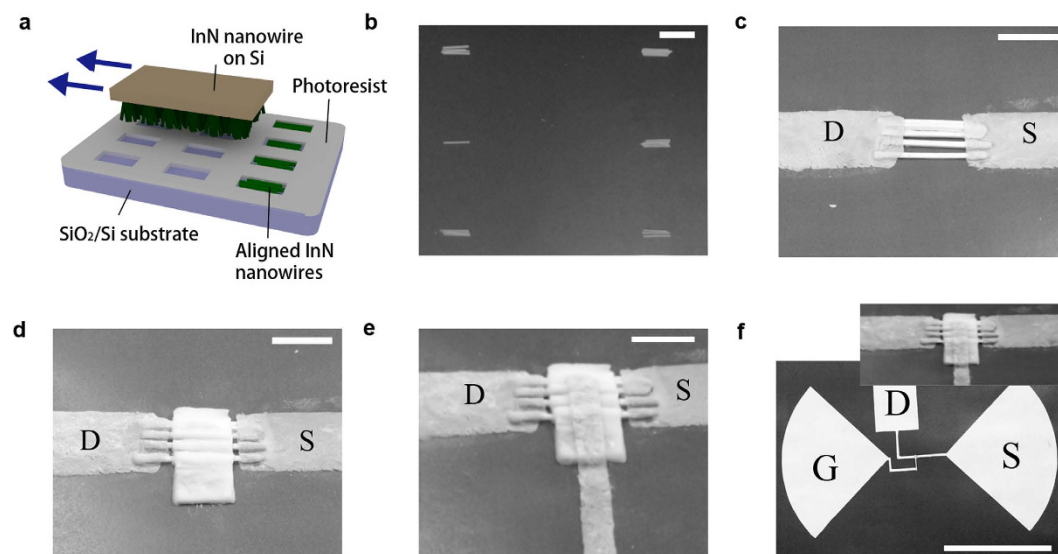


**Figure 6.** (**a**) Schematic drawing of the "transfer printing" process. (**b**) SEM image of InN nanowires in array groups derived from "transfer printing" process. Scale bar: 5μm. (**c**) SEM image of the aligned nanowires with source and drain electrodes deposited. Scale bar: 2μm. (**d**) SEM image of the nanowire device with gate 300 nm $Al_2O_3$ deposited. (**e**) SEM image of the nanowire FET based on 5 aligned nanowires. Scale bar: 2μm. (**f**) SEM image of the whole device. Scale bar: 100μm.

the transfer-printing process. In the following FET device fabrication, one group containing 5 nanowires was selected for demonstration. Source, drain (10 nm Ti/20 nm Au) were defined and deposited by photolithography and e-beam evaporation (Fig. 6c) to two heads and tails of the nanowires. The gate area was defined by photolithography and then 300 nm thick $Al_2O_3$ gate insulator was deposited by e-beam evaporation (Fig. 6d). The gate electrode (50 nm Pt) is finished by the assistance of focused ion beam (FIB) technique (Fig. 6e). Bow-shaped antenna with radius of 100μm was designed to partially resonant with incidence THz wave, while the left and right lobes of the antenna were connected to source and gate electrodes, respectively. The final device structure is also seen in Fig. 6f. The reason of the typical un-symmetric source-drain electrode is for rectifying enhancement to maximize the photovoltage readout.

With the above device geometry, FET characterizations on a single array which consists of 5 InN nanowires were performed at room temperature. The source-drain current ($I_{DS}$) versus source-drain voltage ($V_{DS}$) curves under different gate voltages ($V_G$) $-10$ V to $10$ V is shown in Fig. 7a. $I_{DS}$ increases with the increase of $V_G$ evidently, suggesting typical n-type channel characteristics[29]. Fig. 7b shows the $I_{DS}$-$V_G$
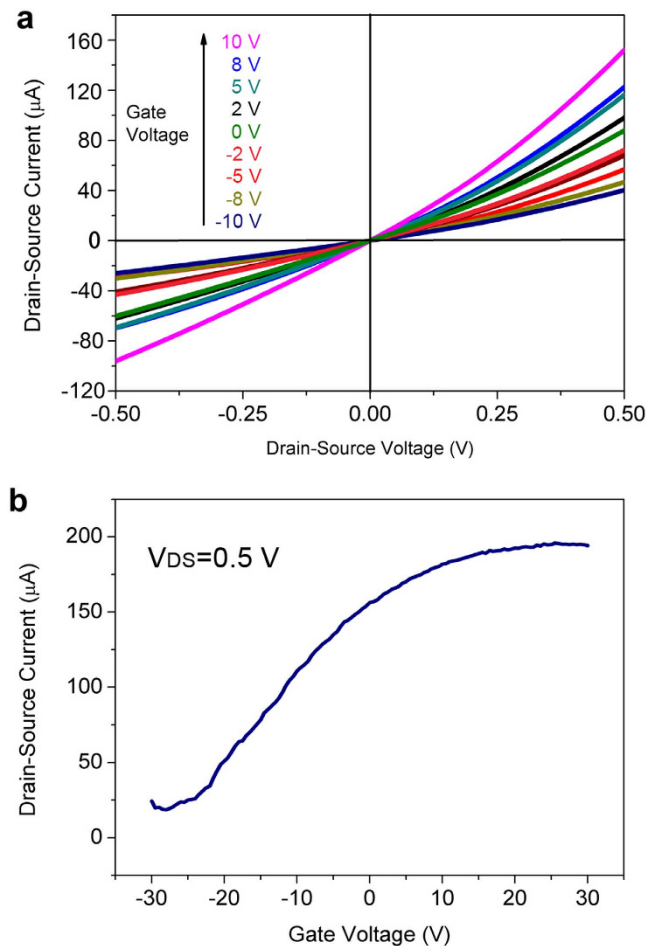
**Figure 7.** (**a**) $I_{DS}$ vs $V_{DS}$ curve of the FET device under different $V_G$. (**b**) $I_{DS}$ vs $V_{DS}$ curve when $V_{DS}$ kept at 0.5 V.

transfer curve at $V_{DS} = 0.5$ V. It is observed that the $I_{DS}$ increases with the increase of $V_G$ from $-30$ V to 30 V, which is in accordance with Fig. 7a. It is notes that with high $V_G$, $I_{DS}$ increase becomes nonlinear, which is possibly due to high current ($\sim 30\mu$A in one nanowire) annealing effect. Also the corresponding $I_{DS}$ at given $V_G$ is not well matched between Fig 7a,b, which is attributed to the hysteresis behavior of the $I_{DS}$-$V_G$ curve. Unlike ZnO nanowire FETs[29] or carbon nanotubes[30], the device does not exhibit very clear and high on/off ratio. The reason is due to residue carrier density that not swept by $V_G$. The threshold voltage ($V_{th}$) is found to be about $-25$ V $\sim -30$ V. In a nanowire FET, the carrier concentration $n$ can be estimated by using the following equation[31]:

$$n = V_{th}C/q\pi \left(\frac{d}{2}\right)^2 L \tag{1}$$

where L, d, $V_{th}$, and q are the channel length ($\sim 1\mu$m), the nanowire diameter (averagely 200 nm), the threshold voltage of the nanowire FET (equals to $-25 \sim -30$ V), and the elementary charge constant q $= -1.6 \times 10^{-19}$ C, respectively. C is the capacitance of the FET device, which is modeled by electrostatic module of Comsol Multiphysics (COMSOL Inc.) to be $4.07 \times 10^{17}$ F. It is assumed that InN nanowires are with similar electrical properties and it can be assumed that the $V_{th}$ are the same for the analysis. From the equation, the electron concentration is calculated to be $3.64 \sim 4.36 \times 10^{17}$ cm$^{-3}$. The mobility can be calculated through the following equation[31]:

$$\mu = \frac{\partial I_{DS}}{\partial V_G} \frac{L^2}{CV_{DS}} \tag{2}$$

where L $= 1\mu$m is the channel length (gate length); $V_{DS} = 0.5$ V; transconductance $\frac{\partial I_{DS}}{\partial V_G} = 1 \times 10^{-6} A/V$ from the linear region of the $I_{DS}$-$V_G$ curve. After all, the mobility of 99 cm$^2$/VS could be calculated by equation (2), which is on the same order with reported InAs nanowire THz detectors ($\sim 500$ cm$^2$/VS)[32].
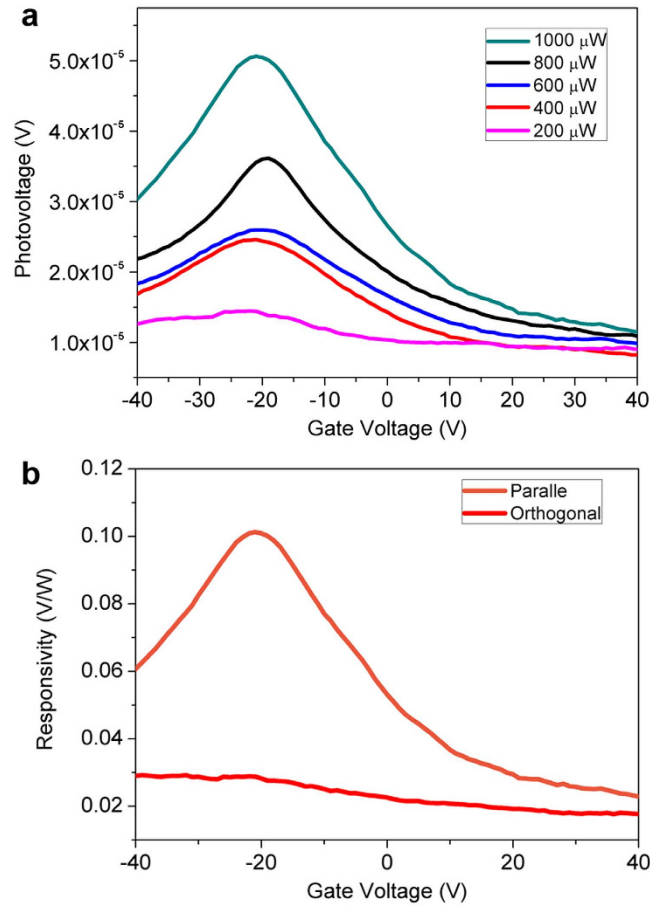
**Figure 8.** (**a**) THz photovoltage as a function of gate voltage under different incidence power. (**b**) Responsivity curves when incidence polarization is paralle (orange curve) or orthogonal (red curve) respect to the antenna.

## Discussion

The THz induced photovoltage vs $V_G$ is depicted in in Fig. 8a. It is observed that there are obvious peaks and the maximums of the photovoltage happen around $-20 \sim -22$ V, which are in proximity with $V_{th}$ in $I_{DS}$-$V_G$ curves. Analysis suggests that this behavior is in accordance with the detection mechanism of a plasmon wave FET detector[33], in which the source-drain photovoltage can be expressed as:

$$\Delta u = \frac{qu_a^2}{4\eta k_B T} \frac{1}{\left[1 + \exp\left(-\frac{qU_G}{\eta k_B T}\right)\right]\left[1 + \kappa \exp\left(-\frac{qU_G}{\eta k_B T}\right)\right]\ln\left[1 + \exp\left(\frac{qU_G}{\eta k_B T}\right)\right]}$$ (3)

Where $q$ is the electron charge, $u_a$ is the small amplitude of the ac wave, $\eta$ is the ideality factor, $k_B$ is the Boltzmann constant, $T$ is the temperature and $U_G$ denotes the gate-to-source voltage minus $V_{th}$ ($U_G = V_G - V_{th}$), and $\kappa = \frac{j_0 L^2 m e}{2C\tau\eta^2 k_B^2 T}$ (here $J_0$ is the gate leakage current density, $L$ is the channel length, $m$ is the electron mass, $C$ is the channel capacitance per unit area, $\tau$ is the momentum relaxation time). Under this circumstance, the maximum of the photovoltage: $\Delta u_{max} \approx \frac{qu_a^2}{4\eta k_B T}$ can be derived at the condition when $U_G = -(\eta k_B T/2)\ln(1/\kappa)$. For different $J_0$, $U_G$ can be on the range of $0 \sim -5$ V[33]. However precise value of maximum point $U_G$ could not be given due to other un-available parameters. Nevertheless, the maximum $U_G$ happens around the point $V_G \approx V_{th}$ with several volts offset, which holds good accordance in the current device data in Fig. 8a. Further, in order to get responsivity values, the following geometric relationship should be taken into account:
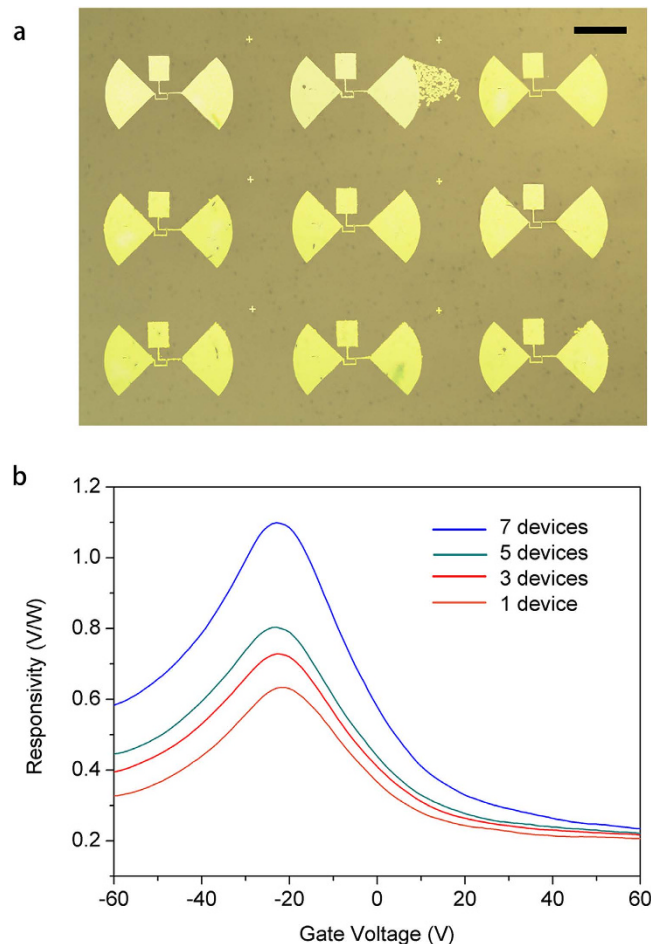
$$R_v = \frac{\Delta u \cdot S_t}{P_t \cdot S_a}$$ (4)

**Figure 9.** (**a**) Microscope image of $3 \times 3$ THz detectors array. Scale bar: $100\,\mu m$. (**b**) Responsivity curves of different number of individual detectors connected in series.

where $R_V$ is the responsivity, $P_t$ is the incidence power impinging on the beam spot, $S_t$ is the radiation beam spot area and $S_a$ is the active area. $S_t = \pi d^2/4 = 1.77 \times 10^{-6}$ m$^2$ and $Sa = \pi R^2/2 = 1.57 \times 10^{-8}$ m$^2$ can be easily calculated. However, the antenna scale is much smaller than the wavelength ($\sim 1\,mm$). So $S_\lambda = \pi \lambda^2/4 = 7.8 \times 10^{-7}$ $m^2$ is taken for the active area. Hence the responsivity spectra at $1000\,\mu W$ with polarization parallel (orange) and orthogonal (red) to the antenna are plotted in Fig. 8b. Obviously parallel measurement yielded much stronger intensity. which is typically due to much higher THz wave absorption rate of the antenna in parallel geometry. Notably, the peak responsivity of the parallel geometry curve reaches $0.1\,V/W$.

The current devices geometry's tremendous advantage lays in the ability of realizing dense array of nanowires THz detectors. Hence the fabrication of pixel-like THz detectors array was done by larger-scale photolithography, transfer-printing and FIB electrodes deposition. A chip carrying $3 \times 3$ detectors is shown in the microscope image of Fig. 9a. Individual detector was designed the same way in Fig. 6. Wire bonding was performed on this chip and successfully enabled 7 operational devices. The active area of the chip is $\sim 1.5\,mm$ in size, which is on the same order of the incidence THz wavelength. On this chip, if more than two detectors are connected in series, it is naturally possible to render stronger photovoltage output. Responsivity characterization was performed, under the assumption that all incidence wave power were absorbed. The result for different number of devices connection is shown in Fig. 9b. Clearly, 7 devices together give the highest responsivity of $1.1\,V/W$. Notably, the change of responsivity intensity from $1 \sim 5$ devices is not as large as from $5 \sim 7$ devices, which is probably due to diffraction associated non-linear absorption phenomena. Nevertheless, the integration of multiple device not only produced stronger photoresponse, it paved the way for practical applications including focal plane pixel THz camera, high output photoconductive THz emitters, etc.

In summary, we have synthesized the InN nanowires and nano-necklaces on the Si substrate through the CVD process. The InN nanowires part was successfully aligned into micrometer sized trenches for controllable nanowire device fabrication. Then remarkable FET characteristics of aligned InN nanowires devices were presented and $99\,cm^2/VS$ electron mobility were achieved. The FET detector rendered $0.1\,V/W$ peak responsivity, while multiple arrays of these detectors were able to be connected to increase

the responsivity to 1.1 V/W. The results demonstrate that aligned InN nanostructures are promising for practical THz applications.

## Methods

**InN nanostructures growth.** The InN nanostructures were synthesized in a horizontal three-temperature zones tube furnace system. A quartz boat containing 0.4 g of In powder (99.999%, Xiya Reagent) was placed in the middle of the II-temperature zone in the closed furnace. An 1.5 cm × 1.5 cm silicon substrate coated with a 60 nm gold colloid (BBI Solution) catalyst film was inversely placed on top of the quartz boat. In another word, the substrate with gold colloid side faced downward, in order to facilitate the growth of nanomaterials. The carrier gas, argon (99.999% purity, Messer), was introduced at one end of the quartz tube at a constant flow rate of 100 sccm (standard cubic centimeters per minute). The I and II temperature zones of the furnace were simultaneously increased to 700 °C in 30 min. Then the $NH_3$ (99.99% purity, Messer) was introduced at same end of the quartz tube at a constant flow rate of 250 sccm when the setting temperature was reached. The growth was kept for 80 min. After the reaction the furnace was cooled to room temperature, and gray and black-colored products were found covering the silicon substrate.

**Materials characterization.** The morphologies and microstructures of the as-synthesized products were systematically characterized. The XRD data was obtained with a Philips X'Pert PRO diffractometer equipped with Cu Ka radiation ($\lambda = 1.5418$ Å). The accelerating voltage was set at 40 kV, with 40 mA flux in the 2Θ range of 10–90°. The field emission SEM images were obtained on the Model Uitra 55 from Carl Zeiss SMT Pte Ltd Co. Germany, which equipped with energy dispersive X-ray spectra (EDS). The TEM images were obtained on the Model Libra 200 PE (200kV) from Carl Zeiss SMT Pte Ltd Co. Germany.

**PL characterization.** The room temperature spatial resolved PL spectra were carried out on a Model inVia Raman Microscope from RENISHAW Co. UK using a 514 nm laser as the excitation source.

**Nanowire alignment.** First, device substrates (500 nm $SiO_2$ on Si) were patterned by photolithography to define the trenches where nanowires will then be transferred. The trench on photoresist width and spacing can be adjusted by designing different photolithography plate; Second, a nanowire growth substrate was brought into contact with the patterned device substrate (nanowires facing the device substrate). A pressure of ~2 kg/cm² was applied while the growth substrate was slide by several mm. After this, many of the nanowires will detach from growth substrate and transfer to device substrate by inter-molecular forces. Finally, the photoresist layer on device substrate was removed by acetone.

**THz detection characterization.** The source used is a AV1450C (Vendor: CETC) signal generator (30 GHz) with frequency multipliers. The output wave is 290 GHz. The THz source is with adjustable power <1 mW and beam diameter of ~1.5 mm. The FET drain contact was connected to a current amplifier, which converting the current into a voltage signal. The output voltage was read by a lock-in-amplifier. The gate voltage was varied using a home built voltage meter. The detector was mounted on a motorized X–Y translation stage to maximize the measured photoresponse.

## References

1. Tonouchi, M. Cutting-edge terahertz technology. *Nature Photon.* **1,** 97–105 (2007).
2. Wilmink, G. J. & Grundt, J. E. Current state of research on biological effects of terahertz radiation. *J. Infrared Mili Terahz Waves* **32,** 1074–1122 (2011).
3. Sirtori, C., Barbieri, S. & Colombelli, R. Wave engineering with THz quantum cascade lasers. *Nature Photon.* **7,** 691 (2013).
4. Kim, J. H., Polley, A. & Ralph, S. E. Efficient photoconductive terahertz source using line excitation. *Opt. Lett.* **30,** 2490–2492 (2005).
5. Berry, C. W., Wang, N., Hashemi, M. R., Unlu, M. & Jarrahi, M. Significant performance enhancement in photoconductive terahertz optoelectronics by incorporating plasmonic contact electrodes. *Nature Comm.* **4,** 1622–1629 (2013).
6. Cherednichenko, S. *et al.* A room temperature bolometer for terahertz coherent and incoherent detection. *IEEE Trans. Terahz. Sci. Tech.* **1,** 395–402 (2011).
7. Han, S. P. *et al.* InGaAs Schottky barrier diode array detector for a real-time compact terahertz line scanner. *Opt. Express* **21,** 25874–25882 (2013).
8. Preu, S. *et al.* An improved model for non-resonant terahertz detection in field-effect transistors. *J. Appl. Phys.* **111,** 024502 (2012).
9. Fatimy, A. E. *et al.* Plasma wave field effect transistor as a resonant detector for 1 terahertz imaging applications. *Opt. Commun.* **282,** 3055–3058 (2009).
10. Cui, Y., Zhong, Z., Wang, D., Wang, W. U. & Lieber, C. M. High performance silicon nanowire field effect transistors. *Nano. Lett.* **3,** 149–152 (2003).
11. Vitiello, M. S. *et al.* A. Room-temperature terahertz detectors based on semiconductor nanowire field-effect transistors. *Nano Lett.* **12,** 96–101 (2012).
12. Viti, L. *et al.* Nanowire Terahertz detectors with a resonant four-leaf-clover-shaped antenna. *Opt. Express* **22,** 8996–9003 (2014).
13. Pitanti, A. *et al.* Terahetz detection by heterostructed InAs/InSb nanowire based field effect transistors. *Appl. Phys. Lett.* **101,** 141103 (2012).
14. Vicarelli, L. *et al.* A. Graphene field-effect transistors as room-temperature terahertz detectors. *Nature Mater.* **11,** 865–871 (2012).
15. Liu, H., Peng, R., Chu, S. & Chu, S. J. High mobility ZnO nanowires for terahertz detection applications. *Appl. Phys. Lett.* **105,** 043507 (2014).

16. Ascazubi, R., Wike, I., Denniston, K., Lu, H. & Schaff, W. J. Terahertz emission by InN. *Appl. Phys. Lett.* **84,** 4810–4813 (2004).
17. Polyakov, V. M. & Schwierz, F. Low-field electron mobility in wurtzite InN. *Appl. Phys. Lett.* **88,** 032101 (2006).
18. Nam, S. W., Jiang, X. C., Xiong, Q. H., Ham, D. H. & Lieber, C. M. Vertically integrated, three-dimensional complementary metal-oxide-semiconductor circuits. *Proc. Nat. Acad. Sci.* **106,** 21035–21038 (2009).
19. Patolsky, F. *et al.* Detection, stimulation, and inhibition of neuronal signals with high-density nanowire transistor arrays. *Science* **313** 1100–1104 (2006).
20. Sahoo, P. *et al.* Role of surface polarity in self-catalyzed nucleation and evolution of GaN nanostructures. *Cryst. Growth. Des.* **12,** 2375–2381 (2012).
21. Sardar, K., Deepak, F. L., Govindaraj, A., Seikh, M. M. & Rao, C. N. R. InN nanocrystals, nanowires, and nanotubes *Small.* **1,** 91–94 (2005).
22. Ji, X., Cheng, S., Hu, H., Li, H., Wu, Z. & Yan, P. Effect of catalyst nanoparticle size on growth direction and morphology of InN nanowires. *AIP ADVANCES* **2,** 022150 (2012).
23. Wang, H. *et al.* Single-crystal AlN nanonecklaces. *Nanotechnology* **20,** 025611 (2009).
24. Yuan, F. *et al.* Synthesis, microstructure, and cathodoluminescence of [0001]-oriented GaN nanorods Grown on conductive graphite substrate. *ACS Appl. Mater. Interfaces* **5,** 12066–12072 (2013).
25. Glushenkov, A. M., Zhang, H., Zou, J., Lu, G. Q. & Chen, Y. Unusual corrugated nanowires of zinc oxide. *J. Cryst. Growth* **310,** 3139–3143 (2008).
26. Chen, R. S. *et al.* High-gain photoconductivity in semiconducting InN nanowires. *Appl. Phys. Lett.* **95,** 162112 (2009).
27. Lai, F. *et al.* Photoluminescence studies of indium nitride films grown on oxide buffer by metalorganic molecular-beam epitaxy. *J. Cryst. Growth* **320,** 32–35 (2011).
28. Zubrilov, A., Levinshtein, M., Rumyantsev, S. L. & Shur, M. S. *Properties of advanced semiconductor materials: GaN, AlN, InN, BN, SiC, SiGe. Ch. 2, 49-50* (John Wiley & Sons 2001).
29. Fan, Z., Wang, D., Chang, P., Tseng, W. Y. & Lu, J. G. ZnO nanowire field-effect transistor and oxygen sensing property. *Appl. Phys. Lett.* **85,** 5923–5925 (2004).
30. Chen, H., Cao, Y., Zhang, J. & Zhou, C. Large-scale complementary macroelectronics using hybrid integration of carbon nanotubes and IGZO thin-film transistors. *Nature Commun.* **5,** 4097–4109 (2014).
31. Xiang, J., Lu, W., Hu, Y., Yan, H. & Lieber, C. M. Ge/Si nanowire heterostructures as high performance field-effect transistors. *Nature* **441,** 489–493 (2006).
32. Viti, L. *et al.* Nanowire Terahertz detectors with a resonant four-leaf-clover-shaped antenna. *Opt. Exprss.* **22,** 8996–9003 (2014).
33. Knap, W. *et al.* Nonresonant detection of terahertz radiation in field effect transistors. *J. Appl. Phys.* **91** 9346–9353 (2001).

## Acknowledgement

## Author Contributions

X.C. and H.L. contributed equally to this work. S.C., R.P. and B.C directed the project. S.C. proposed and designed the project, X.C., H.L., Q.L. and H.C. carried out the experiment and analyzed the data through discussions with S.C. All the authors discussed the results and contributed to the final version of the manuscript.

## Additional Information

**Competing financial interests:** The authors declare no competing financial interests.

**How to cite this article**: Chen, X. *et al.* Terahertz detectors arrays based on orderly aligned InN nanowires. *Sci. Rep.* **5**, 13199; doi: 10.1038/srep13199 (2015).